AGU PUBLICATIONS

JGR

Journal of Geophysical Research: Solid Earth

RESEARCH ARTICLE

10.1002/2014JB011742

Key Points:
- Most RFPs exhibit westward drift and almost all migrate to higher latitudes
- Advection and diffusion of RFPs explain the historical decrease in the ADM
- Spherical harmonic degrees 4 and above strongly affect the existence of the RFPs

Correspondence to:
F. Terra-Nova,
filipe.terranova@iag.usp.br

Citation:
Terra-Nova, F., H. Amit, G. A. Hartmann, and R. I. F. Trindade (2015), The time dependence of reversed archeomagnetic flux patches, *J. Geophys. Res. Solid Earth*, *120*, 691–704, doi:10.1002/2014JB011742.

Received 5 NOV 2014
Accepted 14 JAN 2015
Accepted article online 20 JAN 2015
Published online 18 FEB 2015

The time dependence of reversed archeomagnetic flux patches

Filipe Terra-Nova[1,2], Hagay Amit[2], Gelvam A. Hartmann[1,3], and Ricardo I. F. Trindade[1]

[1]Departamento de Geofísica, Instituto de Astronomia, Geofísica e Ciências Atmosféricas, Universidade de São Paulo, São Paulo, Brazil, [2]CNRS, Université de Nantes, Nantes Atlantiques Universités, UMR CNRS 6112, Laboratoire de Planétologie et de Géodynamique, Nantes, France, [3]Observatório Nacional, Rio de Janeiro, Brazil

Abstract Archeomagnetic field models may provide important insights to the geodynamo. Here we investigate the existence and mobility of reversed flux patches (RFPs) in an archeomagnetic field model. We introduce topological algorithms to define, identify, and track RFPs. In addition, we explore the relations between RFPs and dipole changes and apply robustness tests to the RFPs. In contrast to previous definitions, patches that reside on the geographic equator are adequately identified based on our RFPs definition. Most RFPs exhibit a westward drift and migrate toward higher latitudes. Undulations of the magnetic equator and RFPs oppose the axial dipole moment (ADM). Filtered models show a tracking behavior similar to the nonfiltered model, and surprisingly new RFPs occasionally emerge. The advection and diffusion of RFPs have worked in unison to yield the decrease of the ADM at recent times. The absence of RFPs in the period 550–1440 A.D. is related to a low in intermediate degrees of the geomagnetic power spectrum. We thus hypothesize that the RFPs are strongly dependent on intermediate spherical harmonic degrees 4 and above.

1. Introduction

The geomagnetic field is generated by convective motions of an electrically conducting fluid in the Earth's outer core. This field is observed directly since about 1590 A.D. by ships, observatories, and more recently at space by satellites [e.g., *Jackson et al.*, 2000; *Jonkers et al.*, 2003; *Hulot et al.*, 2010]. For periods preceding direct magnetic measurements, analysis of archeological and geological materials (indirect observations) provide vital information about the field. At first order, these two kinds of observations show that the field is dominated by an axial dipole. However, some nondipole features are also present, particularly in regions at the core-mantle boundary (CMB) where the polarity is opposite to that of the axial dipole (the so-called reversed flux patches, from hereafter RFPs). Expansion and intensification of these RFPs over at least the past century seem to contribute to the historical decrease in the intensity of the dipole moment [*Gubbins*, 1987].

Changes in the dipole are intrinsically related to the flow patterns of the fluid at the top of the outer core, especially to core flow features near RFPs [*Olson and Amit*, 2006; *Amit and Olson*, 2008]. Most of the radial field at the CMB is negative in the Northern Hemisphere and positive in the Southern Hemisphere. A normal flux patch has the same sign as its hemisphere, whereas an RFP has the opposite sign to its hemisphere. The most intense RFPs over the past decades are observed below the southern Atlantic hemisphere [e.g., *Jackson et al.*, 2000; *Olsen et al.*, 2010]. Direct measurements of the geomagnetic dipole intensity reveal a sustained rapid decrease since 1840 A.D. [*Gubbins*, 1987; *Bloxham and Jackson*, 1992; *Jackson et al.*, 2000; *Gubbins et al.*, 2006; *Olson and Amit*, 2006; *Finlay*, 2008]. Dipole secular variation (SV) contributes substantially to the observed field variation at Earth's surface, in particular, the steady decrease in dipole intensity over historical times. Therefore, understanding the dipole SV is crucial to understanding and perhaps predicting how the field evolves. However, it is worth noting that at its source, the CMB, dipole SV constitutes a very small part of the total SV: The SV spectrum is "blue," i.e., its power increases with harmonic degree (smaller scales).

The geomagnetic dipole intensity has been investigated using maps of the spatial contributions to the axial dipole [*Gubbins*, 1987; *Gubbins et al.*, 2006]. The temporal variability in the integrated contribution of reversed flux to the axial dipole balances its total change [*Olson and Amit*, 2006], emphasizing the role of RFPs in the decrease of dipole intensity over the historical era. However, the role of RFPs in dipole changes over millennial timescales has not yet been explored.

Previous analyses of archeomagnetic field models were mostly carried out on the kinematics of high-latitude intense normal polarity flux patches. These patches were found to be mobile with alternating eastward-westward drifts [*Dumberry and Finlay*, 2007; *Wardinski and Korte*, 2008; *Korte and Holme*, 2010]. *Amit et al.* [2010] designed an algorithm for identification and tracking of intense flux patches in numerical dynamos. *Amit et al.* [2011] applied a similar algorithm for intense archeomagnetic flux patches. They found more westward drift in the Southern Hemisphere than in the Northern Hemisphere, which may indicate the impact of core-mantle thermal coupling on the geodynamo. None of these studies identified and tracked reversed archeomagnetic flux patches.

Based on theoretical arguments and numerical dynamo models, high-latitude intense normal polarity flux patches and RFPs are thought to reflect distinctive dynamical mechanisms. Rapid rotation effects in the outer core yield a flow barrier and surface convergence at the latitudes of the inner core tangent cylinder [*Aurnou et al.*, 2003]. In an α^2 dynamo, columns of fluid that are nearly invariant in the direction of the rotation axis [*Busse*, 1970] intersect the CMB at these tangent cylinder latitudes [*Olson et al.*, 1999]. Downwelling associated with columnar cyclones [*Olson et al.*, 2002; *Amit et al.*, 2007] concentrate magnetic flux to produce the high-latitude intense patches [*Olson and Christensen*, 2002]. The mobility of these robust field structures may be linked to the motion of the vortices [*Amit et al.*, 2010], so their longevity may therefore maintain the axial dipole dominance. In contrast, low- and middle-latitude RFPs could be related to the expulsion of toroidal magnetic field by deep upwelling and radial diffusion below the CMB [*Bloxham*, 1986]. If persistent, such local processes may eventually lead to a global polarity reversal [*Aubert et al.*, 2008]. These distinctive dynamo processes motivate examining the time dependence of RFPs, to compliment previous studies that described the mobility of high-latitude intense normal polarity flux patches [*Dumberry and Finlay*, 2007; *Wardinski and Korte*, 2008; *Amit et al.*, 2011].

In this paper we introduce topological algorithms to define, identify, and track RFPs. We use the CALS3k.4b archeomagnetic field model constructed for the past three millenia [*Korte and Constable*, 2011]. We explore the relation between RFPs temporal evolution and dipole changes. The robustness of the archeomagnetic RFPs is tested to assess the reliability of the identification and tracking results.

2. Methods

2.1. Identification and Tracking

The reversed flux patches (RFPs) identification method at each snapshot comprises four steps. First, the magnetic equator is identified. Second, each grid point is associated with a magnetic hemisphere. Third, peaks of RFPs are identified. Finally, an intensity criterion is invoked to filter out weak insignificant RFPs.

RFPs on the CMB are commonly defined as positive/negative radial field structures in the Northern/Southern Hemispheres [e.g., *Olson and Amit*, 2006]. This definition might be problematic. For example, a patch residing on the geographic equator is considered partly normal partly reversed. We therefore seek a more appropriate definition. In this paper, we use the magnetic equator to define the polarity at each grid point. We coded an algorithm to map the magnetic equator. At a given longitude on the CMB, the magnetic equator is defined as the point where the radial geomagnetic field B_r changes sign. To distinguish between sign changes associated with the magnetic equator or with an RFP, the algorithm searches first a longitude where there is just one point of change in the sign of B_r. This point is guaranteed to be the magnetic equator. From this initial location of magnetic equator, the algorithm selects the closest point on the neighbor longitude which has a change in sign of B_r.

After mapping the magnetic equator we define the magnetic hemispheres. Every grid point north/south of the magnetic equator is assigned to its respective magnetic hemisphere. A difficulty arises at some longitudes where the magnetic equator appears more than once. An algorithm marches from colatitude 0° to 180°, assigning the northernmost point to the northern magnetic hemisphere. Then, after every crossing of the magnetic equator, the next point is assigned to the opposite hemisphere.

Once each point on the CMB is associated with a magnetic hemisphere and a polarity (normal or reversed), the next step is to identify the peaks of RFPs. For this purpose we coded an algorithm to determine field maxima and minima of flux patches at the CMB. The algorithm searches the maxima and minima of the radial field by comparison with neighboring cells. A grid point is considered to be a maximum/minimum if it has higher/lower value than its eight neighboring cells. Maximum or minimum values indicate the coordinates (colatitude and longitude) of the peak of the RFPs at the CMB.

For the final identification step we imposed a criterion of threshold intensity to avoid interpreting insignificantly weak extreme points. For every snapshot, only RFPs with peak values larger than half the most intense RFP of the same snapshot were considered. Obviously, only snapshots with more than one RFP were affected by this criterion.

To track RFPs in time, we coded an algorithm that calculates the distance of each RFP to all RFPs in the next snapshot. The spherical distance is calculated along a great circle. A critical distance was set based on typical large-scale core flow values from geomagnetic secular variation inversions. In the core flow model of *Amit and Olson* [2006], the maximum of time-averaged flow plus 1 standard deviation is about 70 km/yr. We used this value multiplied by the time step between snapshots of 10 years to obtain the critical distance for tracking. A pair of RFPs at two successive snapshots which has a spherical distance lower than this critical value is denoted as the same RFP. If an RFP in the new snapshot is farther from all previous snapshot's RFPs than the critical distance, it is denoted as a new RFP.

2.2. Dipole Changes

We took advantage of the above definitions to map local contributions to the axial dipole moment (ADM), and we investigated the temporal behavior of these contributions. The axial component of the magnetic dipole moment (m_z) is defined as follows [*Moffatt*, 1978; *Gubbins*, 1987; *Gubbins et al.*, 2006; *Olson and Amit*, 2006]:

$$m_z = \frac{4\pi a^3}{\mu_0} g_1^0 = \frac{3r_o}{2\mu_0} \int_S B_r \cos\theta \mathrm{d}S \tag{1}$$

where a is the radius of the Earth, $\mu_0 = 4\pi \times 10^7$ Hm^{-1} is the free space magnetic permeability, g_1^0 is the axial dipole Gauss coefficient, r_o is the radius of the core, B_r is the radial component of the magnetic field on the CMB, θ is colatitude and dS denotes a CMB surface increment. The integrand $B_r \cos\theta$ represents the spatial distribution of local contributions to the ADM. Thus, mapping $B_r \cos\theta$ allows imaging local contributions to the ADM.

We associate different types of $B_r \cos\theta$ structures to different ADM contributions as:

$$m_z = m_{n+} + m_{n-} + m_{r+} + m_{r-} \tag{2}$$

where the subscripts n and r denote contributions from regions of normal and reversed flux respectively, m_{n+} represents reinforcing contributions (mostly from high-latitude flux patches), m_{n-} corresponds to opposite contributions (totally from magnetic equator undulations), m_{r+} represents reinforcing contributions and m_{r-} denotes opposite contributions. Note that m_{r+} contributions appear when an RFP is localized at least partly between the magnetic equator and the geographic equator.

2.3. Robustness Tests

Uncertainties in archeomagnetic field models will produce erroneous results concerning the existence and mobility of RFPs. Robustness tests are clearly required. Two tests were performed, one using the power spectrum, the other using low-pass-filtered fields.

The Mauersberger-Lowes spectrum at the CMB is one of the primary outputs of the dynamo process in the core [*Dormy et al.*, 2000]. The magnetic field spectrum R_n at the CMB can be expressed as a function of spherical harmonic degree n in terms of the Gauss coefficients of the core field as [*Lowes*, 1974]:

$$R_n = (n+1)\left(\frac{a}{r_o}\right)^{2n+4} \sum_{m=0}^{n} \left(g_n^m\right)^2 + \left(h_n^m\right)^2 \tag{3}$$

where n is degree, m is order, and the sets g_n^m and h_n^m are the Gauss coefficients. We compared the spectrum at periods without RFPs with the spectrum at periods with RFPs to test whether the absence of patches is due to low field resolution manifested by a steeper descending spectrum.

In the second test, we defined a low-pass filter $F(n)$ by

$$F(n) = \begin{cases} 1 & , \text{ if } n < n_0 \\ cos\left(\frac{n-n_0}{n_f-n_0} \cdot \frac{\pi}{2}\right) & , \text{ if } n \geq n_0 \end{cases} \tag{4}$$

where n_0 marks the beginning of the filtering and n_f marks the truncation. At $n = n_f$ the filter $F(n_f) = 0$, so the highest degree considered is $n_f - 1$. We examined the sensitivity of the identification and tracking

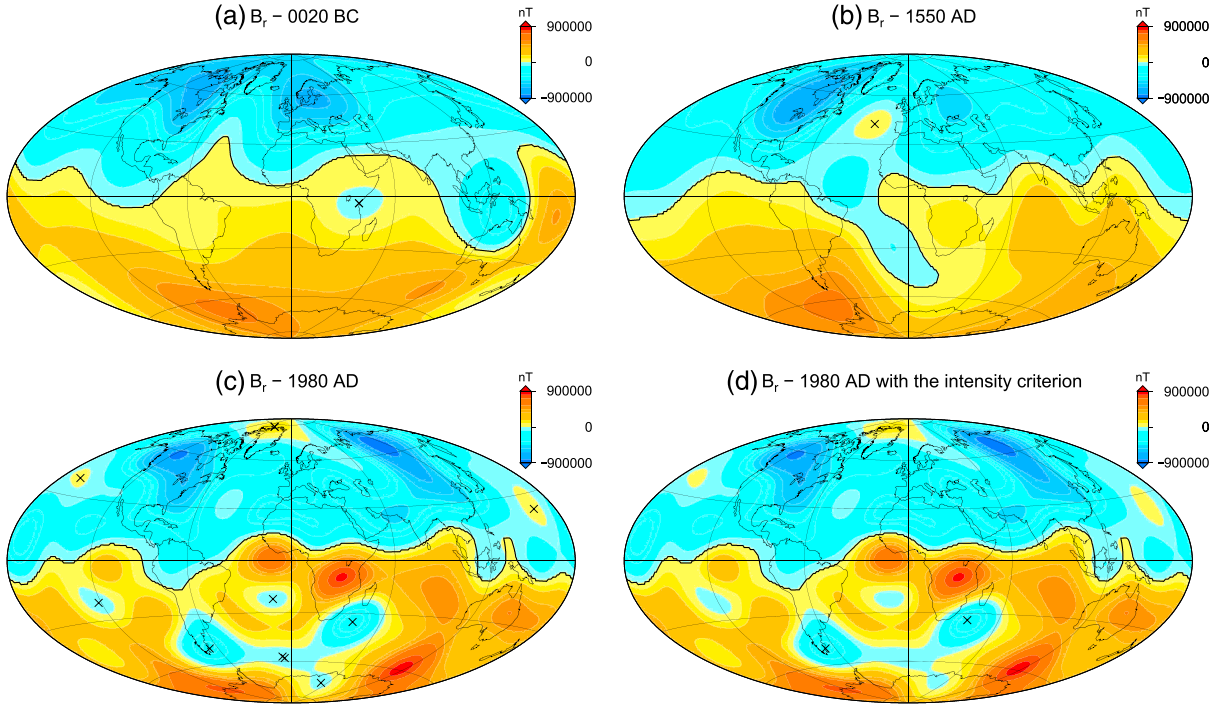

Figure 1. Radial geomagnetic field on the CMB at (a) 0020 B.C., (b) 1550 A.D., and (c) 1980 A.D. based on the CALS3k.4b archeomagnetic field model of [*Korte and Constable*, 2011]. The black line is the mapped magnetic equator, and the black X symbols are the peaks of the RFPs. (d) The RFPs identification for 1980 A.D. with the intensity criterion.

of RFPs to the small-scale field, which is most uncertain in the archeomagnetic field models, by comparing our results using the nonfiltered archeomagnetic field model with those obtained using different low-pass-filtered field models. Finally, we compare our results with the same analysis based on the historical field model GUFM1 [*Jackson et al.*, 2000] to further assess the robustness of the results from the archeomagnetic models.

3. Results

3.1. Identification and Tracking

We used the CALS3k.4b model of *Korte and Constable* [2011] for the interval 990 B.C. until 1990 A.D. This model was constructed from intensity and direction data acquired in archeological (potteries, bricks, etc.) and geological (basaltic flows and lake sediments) materials. In addition, this model is constrained by GUFM1 [*Jackson et al.*, 2000] from 1840 onward, the latter inverted from direct measurements from observatories and satellites. The database used in this model is an extension of the previous compilation of *Korte et al.* [2009]. Consequently, this model presents an improvement in the fit of the Gauss coefficients due to database updates. The model is expanded up to spherical harmonic degree 10 and the temporal resolution is 10 years. We used a regular grid on the CMB of 1° in longitude and latitude.

Figure 1 illustrates the performance of our identification algorithm using three snapshots of the radial archeomagnetic field model on the CMB. The magnetic equator is marked by a solid black line, and each identified RFP is marked by an X symbol (see Figure 1). Our algorithm for mapping the magnetic equator resolves well the magnetic hemispheres, defines local polarity, and correctly identifies RFPs that reside on the geographic equator. Therefore, RFPs are never considered partly normal partly reversed. Figure 1a shows an example of a successfully identified RFP that resides on the geographic equator below eastern Africa.

Figure 1b shows an example of an especially complicated case for the mapping of the magnetic equator. For some longitudes the magnetic equator is crossed 3 times (in other rare snapshots not shown here up to five such crossings occurred). In addition, the magnetic equator penetrates up to a relatively high latitude. Nevertheless, our algorithm correctly maps the magnetic equator. Although the field morphology of the snapshot in Figure 1b is somewhat extreme, in many snapshots of the studied period a significant deviation

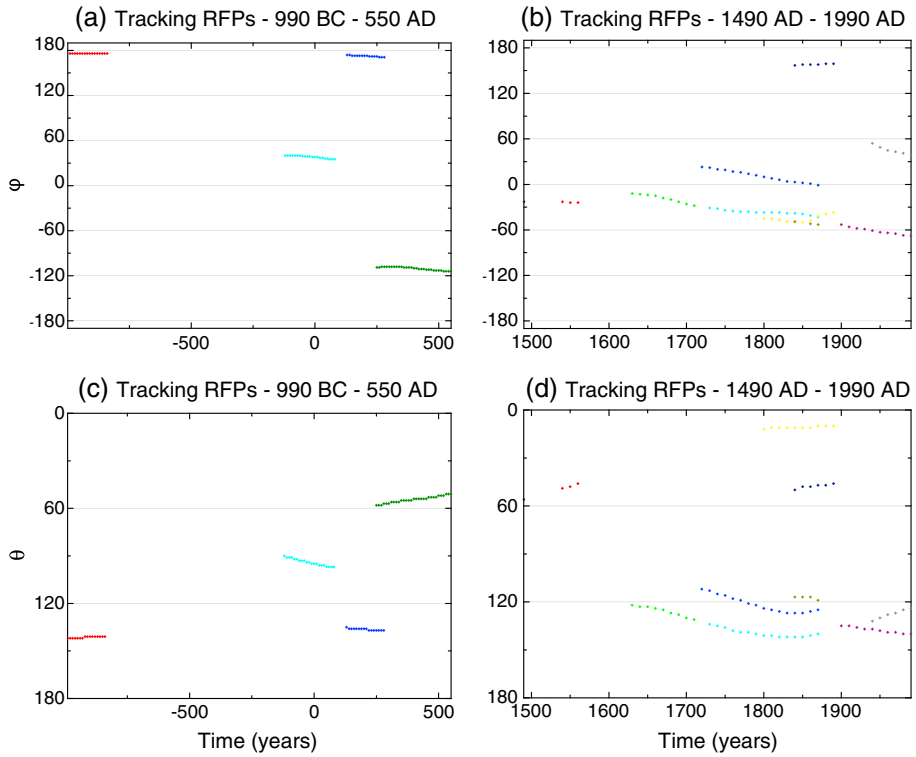

Figure 2. Temporal evolution of the (a, b) longitude, and (c, d) colatitude of peaks of intense RFPs in the model CALS3k.4b [*Korte and Constable*, 2011]. Figures 2a and 2c are from 990 B.C. to 550 A.D.; Figures 2b and 2d are from 1490 A.D. to 1990 A.D. The same colors are used for longitude and colatitude of a given RFP. Longitudes and colatitudes are given in degrees. All curves are dotted; In Figures 2a and 2c the dotted lines seem solid due to the large period covered.

of the magnetic equator from the geographic equator appears. The identification of magnetic hemispheres allowed the straightforward mapping of regions of reversed flux. Furthermore, deep intrusions of normal polarity field to the opposite hemisphere as a result of undulations of the magnetic equator were correctly interpreted as normal flux. This is exemplified by a large normal polarity intrusion south of the geographic equator but north of the magnetic equator that is correctly identified as a region of normal flux in Figure 1b.

Some RFPs are very weak, as evidenced in Figure 1c. Two of these peaks (at high latitudes of the southern Atlantic Ocean) are very close to each other. Accounting for these weak peaks might bias the tracking of RFPs. We therefore introduced in Figure 1d the intensity criterion (compare Figures 1c and 1d). Figure 1d contains two peaks of intense RFPs in the Southern Hemisphere. These two RFPs are part of a large area of reversed flux over the Atlantic Ocean, South America, and Antarctica.

The tracking of RFPs that pass the intensity criterion is separated into intervals with different RFPs activity. For all intervals, we tracked longitude and colatitude (Figure 2). The first interval is from 990 B.C. to 550 A.D. (Figures 2a and 2c) and the second from 1450 A.D. to 1990 A.D. (Figures 2b and 2d). No patches were observed between these two intervals, comprising the period 550 A.D.–1440 A.D. in Figure 2. From 990 B.C. to 550 A.D., four RFPs were identified and tracked. In this period, we found two nearly stationary RFPs (red and blue) and two with westward drift (green and cyan). The latter two RFPs exhibit motion toward higher latitudes. From 1450 A.D. to 1990 A.D. the field model is characterized by higher spatial resolution resulting in a much higher occurrence of RFPs. Most RFPs exhibit a westward drift, but some quasi-stationary RFPs are also observed. In addition, most RFPs migrate toward higher latitudes.

We quantified the statistical behavior of RFPs. Table 1 shows the average rate of azimuthal displacement per year for three types of motions: quasi-stationary, westward, and eastward. The critical azimuthal angular velocity distinguishing drift from quasi-stationary is the quarter of the weighted average of all RFPs, with the weighting being proportional to the lifetime of each RFP. We did not take the average minus 1 standard

Table 1. Types of RFPs Azimuthal Motions and the Rate of Their Displacement per Year[a]

	Nonfiltered		f8/11		f5/11		f3/8	
	N_{RFPs}	Rate	N_{RFPs}	Rate	N_{RFPs}	Rate	N_{RFPs}	Rate
Quasi-stationary	2	−0.01	3	−0.01	4	−0.01	2	−0.02
Westward	9	−0.10	10	−0.09	8	−0.09	3	−0.17
Eastward	2	0.07	1	0.02	2	0.04	0	0

[a] N_{RFPs} is the number of RFPs. The f8/11, f5/11, and f3/8 are filtered models in spherical harmonic degrees between 8 and 11, 5 and 11, and 3 and 8, respectively. Each rate is given in °/*yr*. Quarter of the average of rate is the critical value to distinguish quasi-stationary and drifting features.

deviation because the distribution of RFPs azimuthal angular velocity turns out to be non-Gaussian. RFPs that have angular velocity higher than this critical value are considered drifting. Table 1 indicates that the RFPs exhibit more a westward drift than other kind of azimuthal motions. Quasi-stationary motion occurs much less and the number of RFPs with eastward drift is the lowest. Finally, the rate of westward drift is significantly larger than the rate of eastward drift.

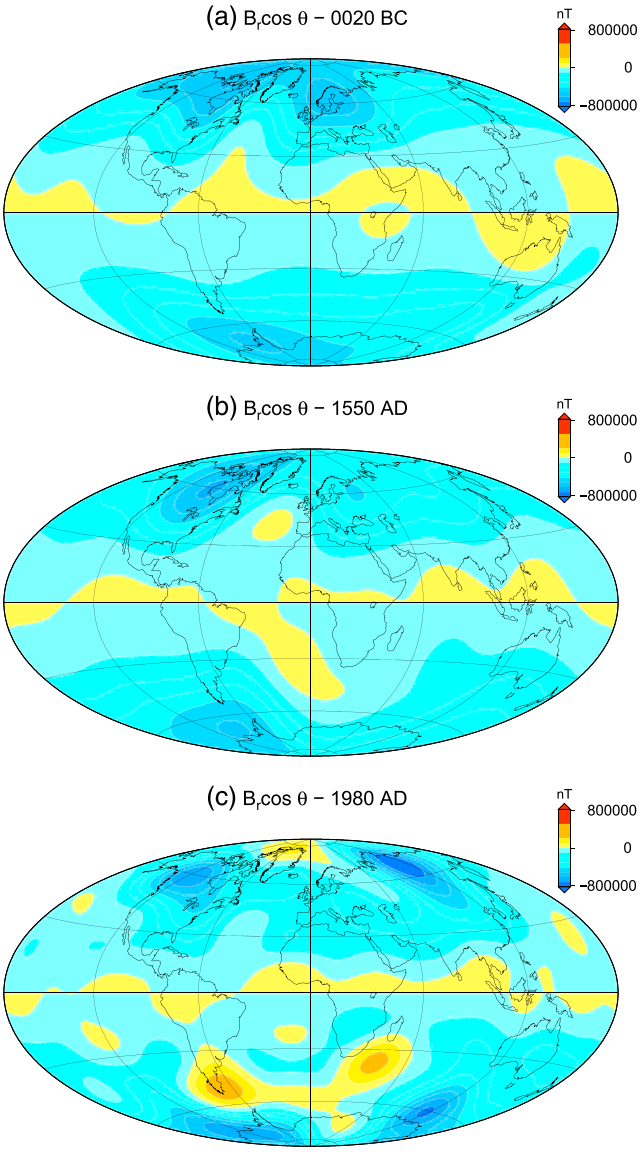

Figure 3. Local contributions to the ADM $B_r \cos\theta$ at (a) 0020 B.C., (b) 1550 A.D., and (c) 1980 A.D.

3.2. Dipole Changes

Spatial contributions (by normal or reversed flux) to the ADM were mapped using the integrand of equation (1), $B_r \cos\theta$. Positive values denote opposite contributions to ADM, while negative values denote reinforcing contributions. Figure 3 shows local contributions to the ADM in the same years as in Figure 1. High-latitude intense normal flux patches provide the most important reinforcing contributions to the ADM. Midlatitude RFPs constitute the most significant opposite contributions to the ADM.

The mathematical definition of ADM contributions considers the geographic equator. Consequently, in Figure 3a below eastern Africa contributions from one RFP (Figure 1a) are partly reinforcing partly opposite. Another type of opposite contribution to the ADM corresponds to areas of magnetic equator undulations. This can be seen for example in Figure 3b below the southern Atlantic Ocean, where normal flux associated with deep magnetic equator intrusion (Figure 1b) yields an opposing contribution to the ADM. In Figure 3c there are two regions of significant opposite contribution for the ADM, one below Patagonia and the other below South Africa. These structures correspond to intense RFPs on the CMB (see Figure 1d).

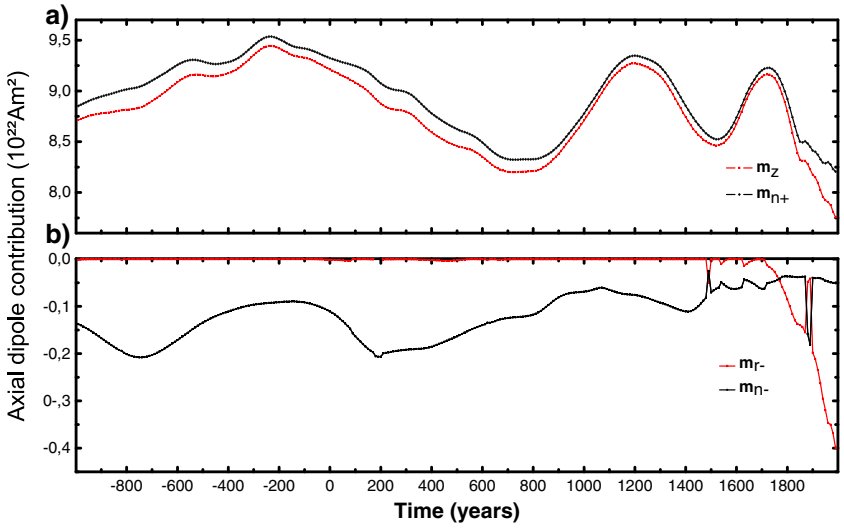

Figure 4. Time dependence of ADM and its different contributions. Values of (a) total m_z and m_{n+} and (b) m_{r-} and m_{n-}. All ADM contributions are expressed in 10^{22} A m^2. Note the difference in scales between Figures 4a and 4b.

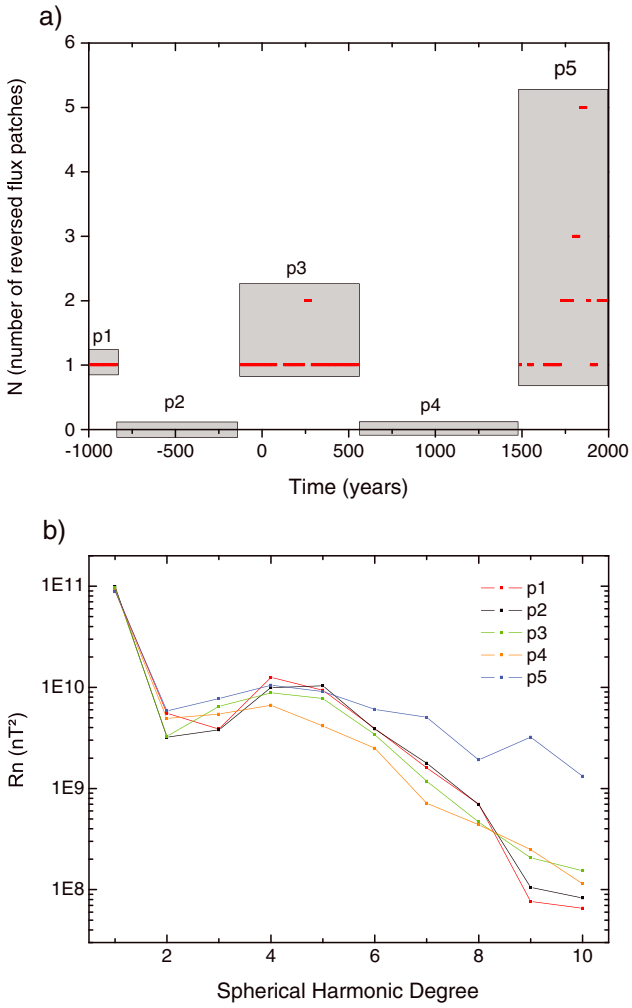

Figure 5. (a) Number of RFPs as a function of time. The five grey rectangles separate five periods. (b) Time-average power spectra for each period in (a).

Figure 4 shows the total ADM (m_z) and its contributions (2), including reinforcing contributions by normal flux (m_{n+}), opposite contributions by normal flux due to magnetic equator undulations (m_{n-}), and opposite contributions by reversed flux (m_{r-}). The reinforcing contributions by reversed flux (m_{r+}) were found to be negligible. The absolute values of m_z and m_{n+} (Figure 4a) are much higher than those of m_{r-} and m_{n-} (Figure 4b), but the temporal variations of the latter contributions are not negligible. From 990 B.C. until about 1800 A.D. the trend of ADM changes is dominantly controlled by high-latitude normal patches. The ADM changes in this period show no correlation with m_{n-} changes. However, the small differences between m_{n+} and m_z are associated with changes in m_{n-}. In 1730 A.D. we detect the most recent local maximum (in absolute value) of m_z and m_{n+} with 9.14×10^{22} A m^2 and 9.23×10^{22} A m^2, respectively (Figure 4a). In 1990 A.D. the corresponding values decreased to 7.75×10^{22} A m^2 and 8.19×10^{22} A m^2, respectively.

Between 990 B.C. and 1760 A.D. RFPs have little impact on ADM changes and m_{r-} is negligible (Figure 4b). The

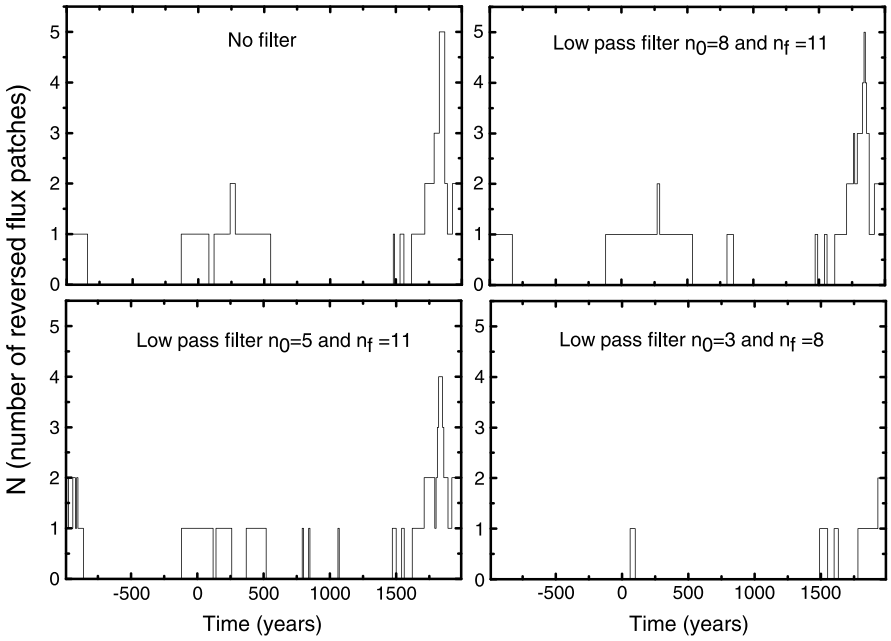

Figure 6. Number of RFPs as a function of time in the filtered field models.

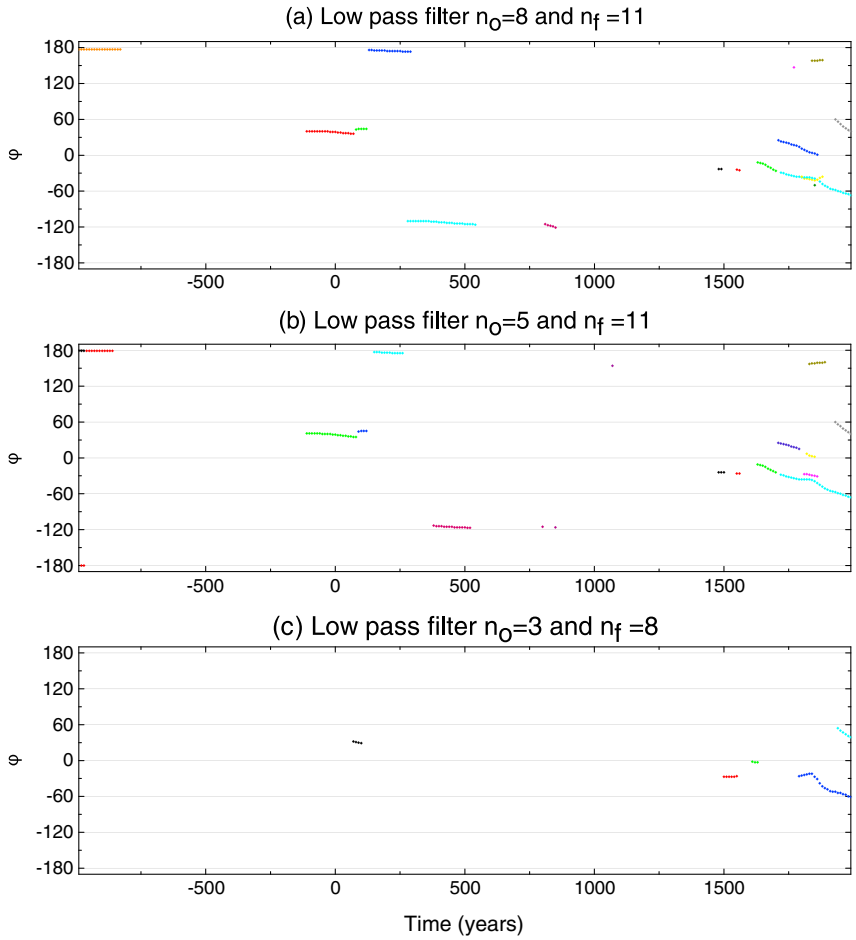

Figure 7. As in Figures 2a and 2b for the filtered field models.

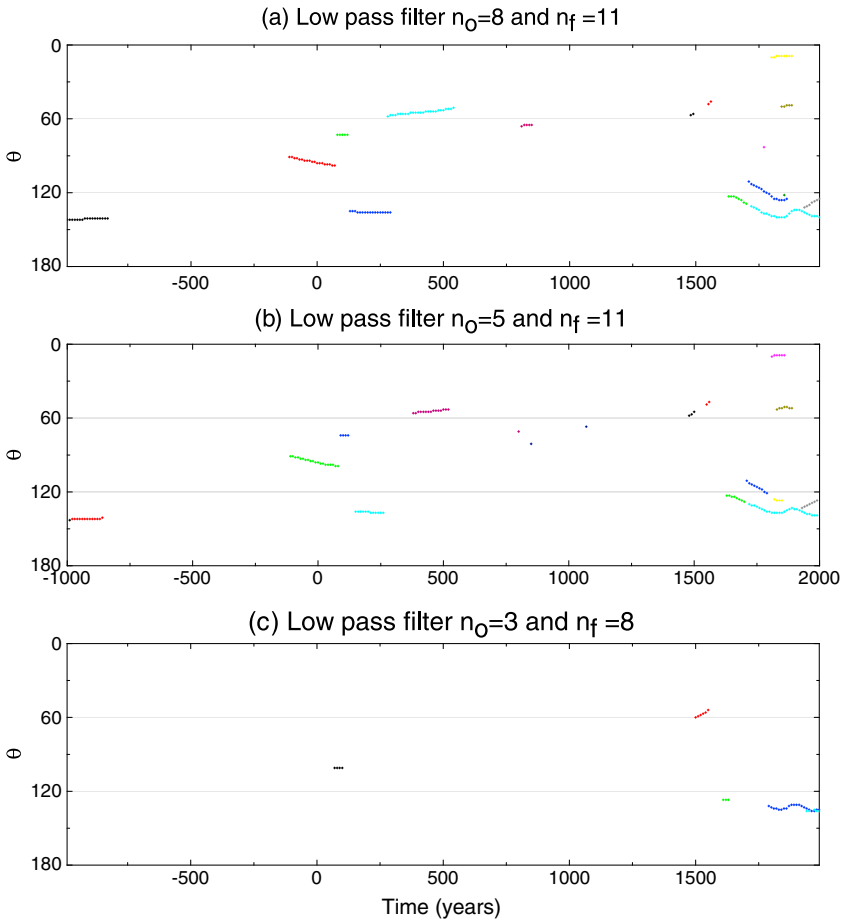

Figure 8. As in Figures 2c and 2d for the filtered field models.

values of m_{n-} are nonnegligible. However, changes of trend and absolute values of m_{n-} are an order of magnitude too low to play a major role in the ADM changes during this period (compare scales between Figures 4a and 4b). The influence of RFPs started to be higher than the influence of magnetic undulations from ~1770 A.D. with increasing trend until 1990 A.D. The m_{r-} absolute value was 0.40×10^{22} A m^2 in 1990 A.D., about 5% of the total ADM in this year. While this absolute value of m_{r-} may seem low, the difference between the total ADM change m_z and the normal flux reinforcing contributions m_{n+} increases from 1790 to 1990 A.D. (Figure 4b) mostly due to the increase in the amplitude of the opposite contributions by m_{r-}.

3.3. Robustness Tests

Figure 5a shows the number of identified RFPs as a function of time. Five periods of time were considered: p1 (990 B.C.–840 B.C.), p2 (830 B.C.–140 B.C.), p3 (130 B.C.–550 A.D.), p4 (560 A.D.–1480 A.D.), and p5 (1490 A.D.–1990 A.D.). In periods p1, p3, and p5 RFPs were found, with p5 having the highest number of RFPs. In periods p2 and p4 no RFPs were found. Figure 5b shows time-averaged power spectra of the intervals identified in Figure 5a. The power spectra exhibit comparable values up to spherical harmonic degree 4. The spectrum in period p4 decreases faster than the others between spherical harmonic degrees 4 and 8. Note that p4 represents almost 1000 years of absence of RFPs. The most recent period p5 has higher values for almost all spherical harmonic degrees. The earlier periods p1, p2, and p3 have a strong decrease of R_n starting in degree 6, and the periods p1 and p2 have the lowest power spectrum values for degrees 9 and 10. Note that the absence of RFPs in period p2 is not reflected in its power spectrum compared to periods p1 and p3.

Next we used low pass filters with three different wave number bands to study the sensitivity of RFPs to uncertain small scales of the field model. The filters are $n_o = 8$ and $n_f = 11$ (denoted f8/11), $n_o = 5$ and

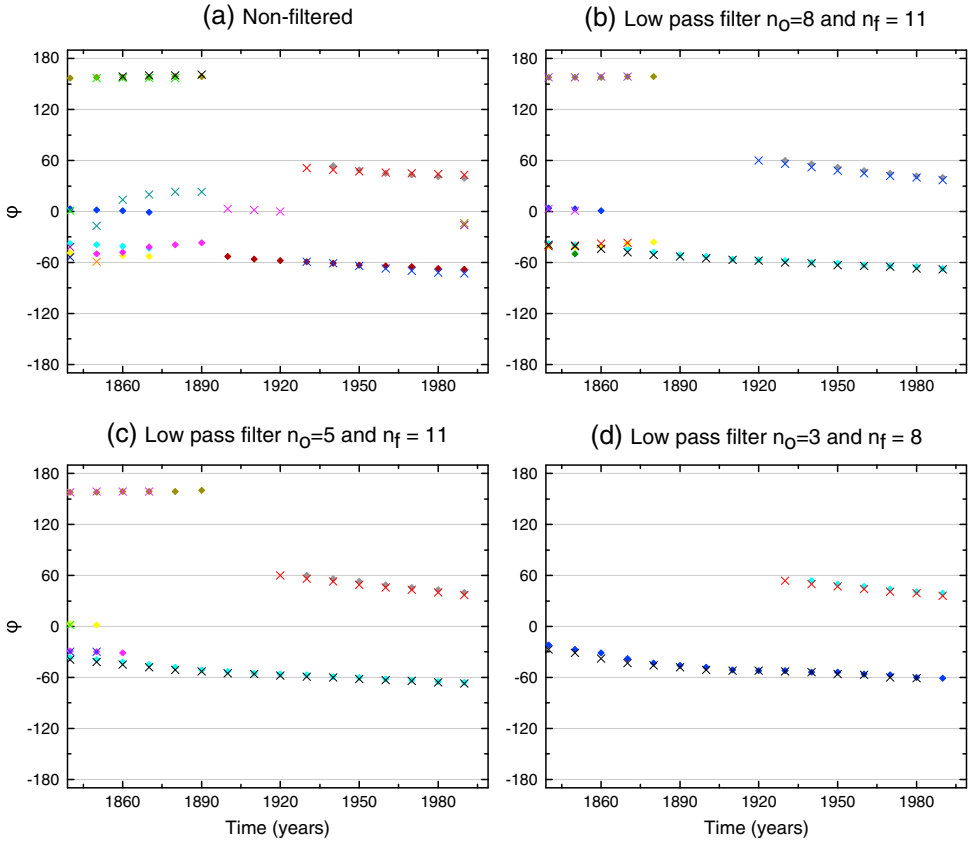

Figure 9. As in Figures 2a and 2b for the period 1840–1990 A.D. for the filtered field models of GUFM1 and CALS3k.4b. Crosses/diamonds represent RFPs of GUFM1/CALS3k.4b respectively.

$n_f = 11$ (denoted f5/11), and $n_o = 3$ and $n_f = 8$ (denoted f3/8) (see (4)). Figure 6 shows that the number of patches per year in filtered models f8/11 and f5/11 was almost the same as that in the nonfiltered model. Filtered model f3/8 has much lower number of patches than the others in all periods. Surprisingly, some new RFPs emerged in models f8/11 or f5/11. Moreover, the total number of patches was even slightly higher in f8/11 than in the nonfiltered model. More specifically note that the large interval of absence of patches (560 A.D.–1480 A.D.) in the nonfiltered model is occasionally abrupt in the filtered models f8/11 and f5/11, even though this interval is characterized by low values of R_n for spherical harmonic degrees higher than 4 (Figure 5b).

We now address the question of how the filters could change the spatial behavior of the RFPs. For this purpose, we tracked in time the coordinates of the RFPs in the filtered models and we compared the results obtained by the different field models (Figures 7 and 8). Figures 2a, 2b, and 7a show similar results between the filtered model f8/11 and the nonfiltered model, with dominance of westward drift. In addition, some new RFPs are occasionally identified and others showed a larger lifetime than in the nonfiltered model. Figure 7b shows that the f5/11 filtered model is also characterized by westward drift and quasi-stationary behavior with most RFPs exhibiting a somewhat shorter lifetime. Figures 7c and 8c show the action of the strongest filter. The low number of RFPs strongly limits the robustness of characterizing their behavior in this model. Only five RFPs were tracked, three of them with westward drift and two were quasi-stationary (Table 1). The time dependence of the colatitude of the RFPs (Figures 2c, 2d, and 8) is rather similar in the nonfiltered, f8/11 and f5/11 models: Most RFPs migrate toward higher latitudes. The most prominent examples include a low-latitude RFP migrating southward between 120 B.C.–80 A.D., a high-latitude RFP moving northward between 210 A.D. and 550 A.D., and several midlatitude RFPs heading southward between 1630 A.D. and the present.

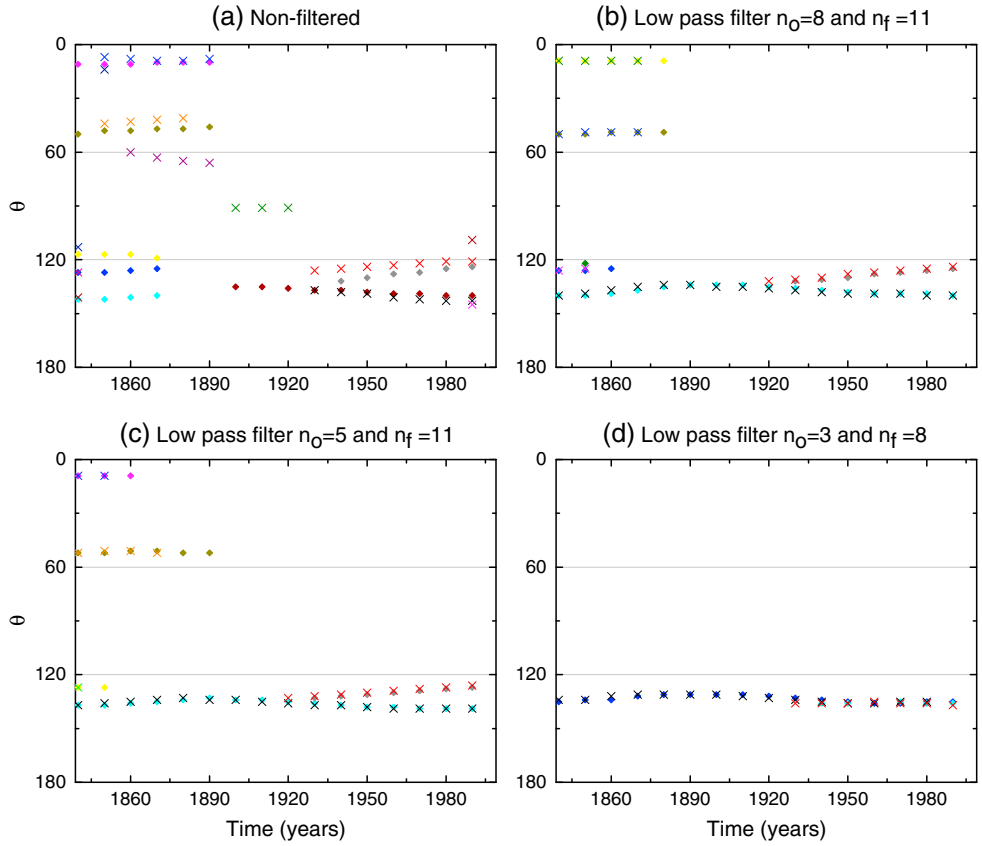

Figure 10. As in Figures 2c and 2d for the period 1840-1990 A.D. for the filtered field models of GUFM1 and CALS3k.4b. Crosses/diamonds represent RFPs of GUFM1/CALS3k.4b, respectively.

3.4. Comparison With the Historical Field

To further test the robustness of the archeomagnetic RFPs, we compare in Figures 9 and 10 results from CALS3k.4b and GUFM1 for the period 1840 to 1990 A.D. Overall, there is a very good agreement between the tracking in both field models. Stronger filters yield even more coincident RFP positions and motions between the two models. As with CALS3k.4b, most RFPs in GUFM1 and their filtered models exhibit westward drift and migrate toward higher latitudes, while some RFPs are characterized by a quasi-stationary behavior.

4. Discussion

Our definition of the local polarity based on the magnetic equator yielded accurate identification of reversed flux patches (RFPs). The intensity criterion filtered out weak RFPs and the velocity criterion connected adequate RFPs in successive snapshots, thus providing meaningful tracking results. Defined this way, RFPs could even be identified on the geographic equator.

One of the earliest and most prominent observations of geomagnetism was the westward drift of field structures [e.g., *Bullard et al.*, 1950; *Yukutake*, 1967; *Bloxham and Gubbins*, 1985; *Finlay and Jackson*, 2003]. Although the core flow is probably more complex, the zonal part of core flow models is often westward at low and middle latitudes, in particular, in the Southern Hemisphere [*Amit and Olson*, 2006]. The dynamical origin of this westward drift is still debated. Recently, it was argued that the westward drift is caused by the gravitational coupling between the inner core and the mantle [*Aubert*, 2013; *Aubert et al.*, 2013]. We find that most RFPs exhibit westward drift. In Table 1, we quantify the azimuthal displacement rate of the RFPs. The westward drifting RFPs move in an average rate of −0.10°/yr, comparable to inferred zonal core flow motions [*Hulot et al.*, 2002; *Holme and Olsen*, 2006]. Tracking in filtered models showed slightly more quasi-stationary RFPs (although still westward drifting RFPs occur more), even though these RFPs have shorter lifetime. The azimuthal displacement rate of the RFPs changes mildly among the different

filtered models, suggesting that the displacement of RFPs is not associated to the highest spherical harmonic degrees. In addition, most RFPs at both hemispheres migrated toward higher latitudes.

We identified different types of possible morphological contributions to the axial dipole moment (ADM) (see Figures 3 and 4). Magnetic equator undulations in early times explain the difference between total ADM and contributions of the intense high-latitude normal flux patches. At recent times, this difference is well explained by opposite contributions of RFPs. The reinforcing contributions of RFPs (which hypothetically may exist) were found negligible. Temporal changes in the intensity and latitude of high-latitude normal flux patches rule exclusively the trend of the ADM when the field is poorly represented in terms of reversed flux regions (likely associated to low resolution of the field model). Finally, RFPs expansion and intensification since 1870 A.D. to present is probably the kinematic signature of radial diffusion at the top of the outer core [*Gubbins*, 1987; *Olson and Amit*, 2006] which may indicate the presence of a thin magnetic boundary layer below the CMB [*Amit and Christensen*, 2008; *Chulliat and Olsen*, 2010].

Changes in the dipole field due to RFPs were only important after 1770 A.D., which is near when CALS3k.4b is constrained by GUFM1. It is likely that RFPs should contribute continually to the dipole field but that low data quality does not allow to resolve them in earlier times. The similar behavior of RFPs in CALS3k.4b and GUFM1 suggests that the spatiotemporal smoothness of the archeomagnetic field model does not prevent identification and tracking of RFPs, but its low resolution reduces the intensity of the RFPs and hence their contribution to the dipole.

Absence of RFPs in the period 550 A.D.–1440 A.D. is related to the low geomagnetic power spectrum in spherical harmonics $n = 4–8$, which is associated with fewer data, resulting in a stronger effect of regularization. However, between 830 B.C. and 140 B.C. the absence of RFPs does not seem to be associated with low geomagnetic power spectrum, because the neighboring periods p1 and p3 (which have similar power spectra as period p2) contain RFPs. The absence of RFPs in this period could therefore genuinely reflect different field morphology and possibly different core dynamics activity in this time interval. The geomagnetic power spectrum for the recent period (p5) is much stronger than that of earlier periods because of the much better coverage and quality of the recent data.

Periods with lower values of geomagnetic power spectrum at high spherical harmonic degree lead to larger-scale field that mask small-scale field structures. Morphologically, it implies that two neighboring regions of opposite flux would be smoothed to one region of the more intense flux. This effect creates undulations in the magnetic equator and obscures RFPs, which limits relating RFPs to ADM changes. Perhaps surprisingly, the filtered models f8/11 and f5/11 show comparable number and more continuous RFPs than in the nonfiltered model. This may be associated to the resolution effects. Another possibility is that two neighboring RFPs, with low intensity values that do not pass the intensity criterion, may merge to one strong RFP after filtering and thus pass the intensity criterion. Note that the large interval of absence of RFPs (560 A.D.–1480 A.D.) in the nonfiltered model is occasionally abrupt in the filtered models f8/11 and f5/11. In these models spherical harmonic degrees 4 and 5 are not filtered whereas higher spherical harmonic degrees 9 and 10 are strongly reduced. Moreover, period p1 has the lowest values of spherical harmonic degrees 9 and 10. These results indicate that spherical harmonic degrees $n = 4–8$ strongly affect RFPs in the archeomagnetic field model. Indeed, the f3/8 filtered model strongly affects intermediate spherical harmonic degrees $n = 4–8$ and contains very few RFPs. Furthermore, period p4 had the lowest values of spherical harmonic degrees $n = 4–8$ compared to the other periods and in this period RFPs are absent (see Figure 5b).

Robust tracking results common to the nonfiltered as well as filtered models may shed light on the kinematics of RFPs. RFPs in all field models exhibit either a westward drift or to a much lesser extent quasi-stationary behavior. In most cases the RFPs drift to higher latitudes, thus systematically weakening the prevailing dipole polarity.

5. Conclusions

Our algorithm allows defining, identifying, and tracking reversed flux patches (RFPs). Our main findings are the following:

1. Most RFPs exhibit westward drift.
2. More than 75% of RFPs migrate toward higher latitudes.

3. In some periods (but not all) the absence of RFPs is due to the low resolution of the field model. Overall, the data are not sufficient to show that the RFPs have not been present at all times in the recent few millennia.
4. Filtered models and comparison with GUFM1 suggest that RFPs are prominent.
5. Spherical harmonic degrees 4 and above strongly affect the existence of the RFPs.

Lastly, we draw attention to the need for new archeomagnetic data to allow for better constrained field models, as well as filters to better select the data used as database to the models. These new models will allow to better identify and track field structures (e.g., RFPs), and consequently to improve the understanding of RFPs and their role in core dynamics on millennial timescales.

Acknowledgments
The field model data for this paper are available at EarthRef.org Digital Archive (ERDA). Data set name: Global archeomagnetic field models CALS3k.4 and CALS3k.4b. Data set link: http://earthref.org/ERDA/1142/. F. Terra-Nova and G. A. Hartmann acknowledge grants 2013/14629-8 and 2010/10754-4, São Paulo Research Foundation (FAPESP), respectively. We would like to thank the Laboratoire de Planétologie et de Géodynamique (LPGNantes/CRNS) and the Instituto de Astronomia, Geofísica e Ciências Atmosféricas (IAG/USP) for the institutional support. This study was partially performed during a 4 month visit of F. Terra-Nova in LPGNantes. We are grateful to Richard Holme and Mathieu Dumberry for their constructive comments that significantly improved the manuscript.

References

Amit, H., and U. Christensen (2008), Accounting for magnetic diffusion in core flow inversions from geomagnetic secular variation, *Geophys. J. Int.*, *175*, 913–924.
Amit, H., and P. Olson (2006), Time-average and time-dependent parts of core flow, *Phys. Earth Planet. Inter.*, *155*, 120–139.
Amit, H., and P. Olson (2008), Geomagnetic dipole tilt changes induced by core flow, *Phys. Earth Planet. Inter.*, *166*, 226–238.
Amit, H., P. Olson, and U. Christensen (2007), Tests of core flow imaging methods with numerical dynamos, *Geophys. J. Int.*, *168*, 27–39.
Amit, H., J. Aubert, and G. Hulot (2010), Stationary, oscillating or drifting mantle-driven geomagnetic flux patches, *J. Geophys. Res.*, *115*, B07108, doi:10.1029/2009JB006542.
Amit, H., M. Korte, J. Aubert, C. Constable, and G. Hulot (2011), The time-dependence of intense archeomagnetic flux patches, *J. Geophys. Res*, *116*, B12106, doi:10.1029/2011JB008538.
Aubert, J. (2013), Flow throughout the Earth's core inverted from gomagnetic observations and numerical dynamo models, *Geophys. J. Int.*, *192*, 537–556, doi:10.1093/gji/ggs051.
Aubert, J., H. Amit, G. Hulot, and P. Olson (2008), Thermo-chemical flows couple the Earth's inner core growth to mantle heterogeneity, *Nature*, *454*, 758–761.
Aubert, J., C. Finlay, and F. Fournier (2013), Bottom-up control of geomagnetic secular variation by the Earth's inner core, *Nature*, *502*, 219–223, doi:10.1038/nature12574.
Aurnou, J., S. Andreadis, L. Zhu, and P. Olson (2003), Experiments on convection in Earth's core tangent cylinder, *Earth Planet. Sci. Lett.*, *212*, 119–134.
Bloxham, J. (1986), The expulsion of magnetic flux from the Earth's core, *Geophys. J. R. Astron. Soc.*, *87*, 669–678.
Bloxham, J., and D. Gubbins (1985), The secular variation of the Earth's magnetic field, *Nature*, *325*, 511–513.
Bloxham, J., and A. Jackson (1992), Time-dependent mapping of the magnetic field at the core-mantle boundary, *J. Geophys. Res*, *97*, 19,537–19,563.
Bullard, E. C., C. Freedman, H. Gellman, and J. Nixon (1950), The westward drift of the Earth's magnetic field, *Philos. Trans. R. Soc. London, Ser. A*, *243*, 67–92.
Busse, F. (1970), Thermal instabilities in rapidly rotating systems, *J. Fluid Mech.*, *44*, 441–460.
Chulliat, A., and N. Olsen (2010), Observation of magnetic diffusion in the Earth's outer core from Magsat, Ørsted and CHAMP data, *J. Geophys. Res.*, *115*, B05105, doi:10.1029/2009JB006994.
Dormy, E., J. Valet, and V. Courtillot (2000), Numerical models of the geodynamo and observational constrains, *Geochem. Geophys. Geosyst.*, *1*, 1037, doi:10.1029/2000GC000062.
Dumberry, M., and C. Finlay (2007), Eastward and westward drift of the Earth's magnetic field for the last three millennia, *Earth Planet. Sci. Lett.*, *254*, 146–157.
Finlay, C. (2008), Historical variation of the geomagnetic axial dipole, *Phys. Earth Planet. Inter.*, *170*, 1–14.
Finlay, C., and A. Jackson (2003), Equatorially dominated magnetic field change at the surface of Earth's core, *Science*, *300*, 2084–2086.
Gubbins, D. (1987), Mechanism for geomagnetic polarity reversals, *Nature*, *326*, 167–169.
Gubbins, D., A. Jones, and C. Finlay (2006), Fall in Earth's magnetic field is erratic, *Science*, *312*, 900–902.
Holme, R., and N. Olsen (2006), Core surface flow modelling from high-resolution secular variation, *Geophys. J. Int.*, *166*, 518–528.
Hulot, G., C. Eymin, B. Langlais, M. Mandea, and N. Olsen (2002), Small-scale structure of the geodynamo inferred from Ørsted and Magsat satellite data, *Nature*, *416*, 620–623.
Hulot, G., C. Finlay, C. Constable, N. Olsen, and M. Mandea (2010), The magnetic field of planet Earth, *Space Sci. Rev.*, *152*, 159–222, doi:10.1007/s11214-010-9644-0.
Jackson, A., A. Jonkers, and M. Walker (2000), Four centuries of geomagnetic secular variation from historical records, *Philos. Trans. R. Soc. London, Ser. A*, *358*, 957–990.
Jonkers, A., A. Jackson, and A. Murray (2003), Four centuries of geomagnetic data from historical records, *Rev. Geophys.*, *41*(2), 1006, doi:10.1029/2002RG000115.
Korte, M., and C. Constable (2011), Improving geomagnetic field reconstructions for 0–3 ka, *Phys. Earth Planet. Inter.*, *188*(3–4), 247–259.
Korte, M., and R. Holme (2010), On the persistence of geomagnetic flux lobes in global field models, *Phys. Earth Planet. Inter.*, *182*, 179–186.
Korte, M., F. Donadini, and C. Constable (2009), The geomagnetic field for 0–3 ka: 2. A new series of time-varying global models, *J. Geophys. Res.*, *10*, Q06008, doi:10.1029/2008GC002297.
Lowes, F. (1974), Spatial power spectrum of the main magnetic field, *Geophys. J. R. Astron. Soc.*, *36*, 717–730.
Moffatt, H. (1978), *Magnetic Field Generation in Electrically Conducting Fluids*, Cambridge Univ. Press, Cambridge, U. K.
Olsen, N., H. Luehr, T. J. Sabaka, I. Michaelis, J. Rauberg, and L. Tøffner-Clausen (2010), CHAOS-4—A high-resolution geomagnetic field model derived from low-altitude CHAMP data, Abstract GP21A–0992 presented at 2010 AGU Fall Meeting.
Olson, P., and H. Amit (2006), Changes in Earth's dipole, *Naturwissenschaften*, *93*, 519–542.
Olson, P., and U. Christensen (2002), The time averaged magnetic field in numerical dynamos with nonuniform boundary heat flow, *Geophys. J. Int.*, *151*, 809–823.
Olson, P., U. Christensen, and G. Glatzmaier (1999), Numerical modeling of the geodynamo: Mechanisms of field generation and equilibration, *J. Geophys. Res.*, *104*, 10,383–11,0404.

Olson, P., I. Sumita, and J. Aurnou (2002), Diffusive magnetic images of upwelling patterns in the core, *J. Geophys. Res.*, *107*(B12), 2348, doi:10.1029/2001JB000384.

Wardinski, I., and M. Korte (2008), The evolution of the core-surface flow over the last seven thousands years, *J. Geophys. Res.*, *113*, B05101, doi:10.1029/2007JB005024.

Yukutake, T. (1967), The westward drift of the Earth's magnetic field in historic times, *J. Geomagn. Geoelec.*, *19*, 93–96.